



DEGREE PROJECT IN TECHNOLOGY,
FIRST CYCLE, 15 CREDITS
STOCKHOLM, SWEDEN 2019

A time alternating classical–quantum method for simulating radiation damage in crystalline materials

DANIEL FRANSÉN



EXAMENSARBETE INOM TEKNIK,
GRUNDNIVÅ, 15 HP
STOCKHOLM, SVERIGE 2019

Klassisk–kvantmekanisk tidsalternerande metod för simulering av strålnings- inducerade defekter i metaller

DANIEL FRANSÉN

Abstract

Radiation damage in metallic components is unavoidable near the core of nuclear fission and fusion reactors. The key parameter for all radiation damage calculations is the threshold displacement energy, commonly determined through molecular dynamics (MD) displacement cascade simulations based on the embedded atom method (EAM), and recently also using the quantum mechanical density functional theory (DFT). DFT is more accurate and provides better agreement with experimental data compared to the considerably much faster EAM. In the present study, the dynamics of DFT and EAM based MD displacement cascade simulations is compared. The differences predominantly appear after 150 to 200 fs or more. A method is therefore proposed which substitutes the first part of a DFT simulation for EAM. The simulation time reduction is considerable due to the low cost of EAM, and due to the fact that a majority of the simulation time is usually spent in the first high energetic collisions which occur in this early part of the collision process. The proposed method is tested by determining the threshold displacement energy and comparing the results to calculations based purely on DFT and EAM. For the tested cascade directions, the method provides good agreement to DFT, including cases where EAM deviates from DFT. With approximately 1/5 of the DFT simulation cost, the proposed alternating EAM-DFT method seems promising but requires further study and verification.

Sammanfattning på svenska – Summary in Swedish

Strålskador i metalliska komponenter är oundvikligt för metaller i reaktormiljöer. Den viktigaste materialparametern för beräkningar av strålningsinducerad defektbildning är tröskelenergin för defektbildning, som ofta bestäms genom molekylodynamiksimuleringar (MD) baserade på den empiriska metoden EAM, och nyligen även den kvantmekaniska metoden täthetsfunktionalteori (DFT). DFT är mer noggrann och har visats ge bättre överensstämmelse med tillgängliga experimentella data, jämfört med den mycket snabbare EAM-metoden. I denna studie undersöks skillnader mellan dynamiken i DFT- och EAM-baserade MD kaskadsimuleringar genom analys av den totala kinetiska energin. Skillnaderna verkar primärt uppstå efter 150 till 200 fs eller mer. En metod föreslås därför som ersätter första delen av en DFT MD simulering med EAM MD. Den möjliga minskningen av beräkningskostnad är stor eftersom den mesta simuleringstiden krävs under de första, högenergetiska kollisionerna, och eftersom EAM har försumbar beräkningskomplexitet jämfört med DFT. Metoden testas genom tröskelenergiberäkningar för ett par riktningar. För de testade fallen ger den föreslagna alternerande EAM-DFT-metoden bra överensstämmelse med DFT, inklusive när EAM och DFT har dålig överensstämmelse. Metoden kan minska simuleringkostnaden till storleksordningen 1/5 av den för DFT, och verkar baserat på de undersökta fallen lovande, men ytterligare undersökning av noggrannheten krävs.

Contents

| | | |
|----------|--|-----------|
| 1 | Background | 5 |
| 1.1 | Lattice defects | 5 |
| 1.2 | DFT and EAM as methods for MD displacement cascade simulations . . . | 8 |
| 1.3 | Density functional theory (DFT) | 8 |
| 1.4 | Embedded atom method (EAM) | 9 |
| 1.5 | DFT - EAM comparison | 9 |
| 2 | Methods | 10 |
| 2.1 | Simulation setup | 10 |
| 2.2 | Implementation | 11 |
| 2.3 | Choosing simulation parameters | 12 |
| 2.4 | Evaluating alternating EAM-DFT qualitatively | 14 |
| 2.5 | Comparing threshold displacement energy calculations | 15 |
| 3 | Results | 16 |
| 3.1 | Evaluating alternating EAM-DFT qualitatively | 16 |
| 3.2 | Determination of TDE in $\langle 110 \rangle$ | 21 |
| 3.3 | Determination of TDE in $\langle 135 \rangle$ and $\langle 30, 5, 2 \rangle$ | 21 |
| 3.4 | Simulation cost | 22 |
| 4 | Discussion | 24 |
| 4.1 | Evaluating alternating EAM-DFT qualitatively | 24 |
| 4.2 | Determination of TDE in $\langle 110 \rangle$ | 24 |
| 4.3 | Determination of TDE in $\langle 135 \rangle$ and $\langle 30, 5, 2 \rangle$ | 25 |
| 4.4 | Limitations and topics of future study | 25 |
| 5 | Conclusions | 26 |
| A | Appendix | 29 |
| A.1 | Density functional theory | 29 |

Acknowledgments

I would like to thank my supervisor Pär Olsson for many interesting discussions, and for giving valuable insights into the computational and radiation damage fields. Also I would like to express my sincere gratitude for his great devotion and guidance in this bachelor thesis project.

Aim and scope

In order to find new alloys with better radiation defect properties, it is crucial to have primary damage simulation methods that are precise and detailed enough to accurately predict differences between materials, but fast enough to be of practical use. In this respect, quantum molecular dynamics (QMD) is the most accurate method for low energy cascade simulations, but it is also quite computationally expensive compared to the less accurate classical molecular dynamics (CMD). It is therefore of interest to investigate if a combination of the two methods could retain most of the benefits of both: a method that is faster than pure QMD but almost as accurate. In the present study, it is investigated if parts of a QMD cascade simulation could be substituted to CMD without losing too much accuracy. The potential reduction of simulation cost is considerable since CMD has negligible computation complexity compared to QMD.

Limitations

Simulating the time evolution of large systems of atoms using QMD is computationally expensive even compared to modern supercomputer standards. Since the computation resources available for the project were restricted, limitations and simplifications over more precise analyses and procedures were necessary. The proposed method is studied for a limited set of cases (energies, lattice directions, etc.) and for one compound using one interatomic EAM potential for the CMD simulations, in addition to the QMD simulations based on density functional theory (DFT). To allow for a reasonably large number of cases to be studied, the simulations were initiated from a stationary system, corresponding to temperature 0K, excepting the primary knock-on atom. Here, for each simulation setup (energy, lattice direction, etc.) only one simulation is needed at 0K, as opposed to nonzero temperatures where a large number of simulations is necessary to gain a statistical basis. The physical implications are mostly small and a good tradeoff to computational cost, and quite acceptable for a first test of a method. Future studies will have to examine remaining aspects induced by the applied limitations.

Considerations on ethics and sustainability

Nuclear energy, including fusion, is an interesting solution to an environmentally friendly and sustainable energy source. New generations of reactors that produce less persistent radioactive waste may provide a solution to the ethic dilemma concerning the long storage time presently needed for used nuclear fuel. One of the main difficulties in the new reactor types is that all known materials are damaged too quickly by the radiation, for components nearest the source. Here, simulations could play a major role by providing a powerful complementary method for development of new materials. Hopefully the result of the present study could contribute to more efficient simulation methods. No other, more direct ethical or societal implications of the present work were found.

1 Background

In nuclear reactors, neutron irradiation causes lattice defects that greatly limit the usable lifetime of the most exposed components, sometimes down to as little as a few years. To enable future development of new materials, and to obtain more accurate radiation damage estimates, basic science today apply increasingly accurate methods where induction of crystal structure defects can be studied. One of the limiting factors is the high computational cost of QMD / DFT MD methods. Below, lattice defects will first be described as a background to what radiation damage is. Subsequently, the damage process from neutron collisions, to the long term mechanical consequences will be described. Lastly, methods for estimating radiation damage will be described, as well as simulation methods that are applied for getting the related material parameters.

1.1 Lattice defects

An ideal crystalline solid exhibits a perfectly regular, translation symmetric structure. Real crystalline materials however contain crystallographic lattice defects that in some respects lead to dramatically different properties compared to the ideal crystal. These lattice defects are categorized according to their dimensionality, from zero-dimensional point defects to often highly complex and varied three dimensional ones. In zero dimensions, there are two basic types. Firstly, a vacancy is an empty lattice site that is normally occupied by an atom. Secondly, an interstitial is an added atom, more generally $n + 1$ atoms sharing the space of n atoms in the corresponding ideal structure. Sometimes, lattice planes may be locally missing, and such defects are referred to as edge dislocations and are of dimensionality one. In two dimensions, a common example of lattice defect is grain boundaries, which are found in polycrystalline materials. Lastly, voids, cracks, and inclusions are common three-dimensional defects [1].

Lattice defects are dynamic and interact in complex mechanisms with major influence on the mechanical properties. Depending on type, lattice defects form through different processes involving mechanical stress and deformation, high temperatures, radiation, and also stochastically due to thermal movements even at low temperatures [1].

1.1.1 Radiation induced lattice defect formation

In nuclear reactors neutron irradiation causes lattice defects that greatly limit the usable lifetime of the most exposed components, sometimes down to as little as a few years. Radiation produces primary damage in materials through collision sequences induced by the energetic neutrons, which results in production of point defects and small point defect clusters. Through secondary damage, the produced vacancies often interact with voids, leading to swelling, and the interstitials often bind to dislocations, inducing dislocation climb which can be described as a spontaneous plastic deformation. Point defects also interact with grain boundaries and through diffusion contribute to segregation of alloying elements in materials with multiple elements [1].

While irradiation damage is a microscopical process, the formation of microscopical defects has major influence on the macroscopic bulk mechanical properties. Weakened grain boundaries, microscopic tensions, voids and decreased dislocation motion due to defect obstacles, all contribute to increased hardness and brittleness, resulting in elevated fracture probability. Also, the swelling caused by void growth is macroscopic and may present issues for example in fasteners (screws, etc), joints, and other high tolerance parts. Furthermore, deformations are sometimes anisotropic even on a macroscopic length scale, primarily in textured materials (polycrystalline materials that exhibit biased crystal directions) [1, 2].

1.1.2 Calculations of radiation damage

Due to the high safety requirements on nuclear reactors, accurate estimates of expected safe operation time of reactor components is paramount. Since point defects are the source of all radiation damage, the starting point for virtually all calculations of irradiation effects is the number of displacements (stable point defects) per atom, dpa (see ref [3] and references therein). Determination of the dpa requires the following to be known:

1. The neutron dose and energy spectrum,
2. the material's neutron cross section, and
3. the number of stable defects produced by a given cascade energy, N_d .

Of these, the last one is most closely related to the topic of the present study. While the first two may be determined experimentally, the mechanisms of single cascades must be simulated due to the small length and time scales. However, since radiation cascades often involve high energies and large number of atoms, direct simulations of full cascades are often impractical or impossible. Empirical methods can, at great cost, simulate full displacement cascades (based on the binary collision approximation or empirical MD). However, these methods still lack in reliable predictive power. Thus, in order for simulations to be of practical use, for example when estimating the lifetime of nuclear components, methods are often applied that estimate the cascade displacements based on more fundamental properties.

For many metals, a first approximation is that the number of point defects induced by a cascade is proportional to the neutron transferred energy. The simplest model for such metals is the Kinchin-Pease model [4], which states that the number of point defects N_d is given by

$$N_d = \begin{cases} 0 & T < E_d \\ 1 & E_d < T < 2E_d \\ T_d/2E_d & 2E_d < T < E_c \\ \text{constant} & T > E_c \end{cases}$$

Here, T is the radiation-transferred kinetic energy and E_d is the threshold displacement energy, the minimum cascade energy required to form a stable defect pair. Also, above

the energy E_c , the model estimates constant defect production due to electron excitation. A more precise model based on that of Kinchin and Pease was later derived in ref. [5]. In this model, the energy T is replaced by the damage energy T_d which is the energy available for atom displacements, and the number of atomic displacements is estimated as

$$N_d(T_d, E_d) = \begin{cases} 0 & T_d < E_d \\ 1 & E_d < T_d < 2E_d \\ \frac{0.8T_d}{2E_d} & 2E_d < T_d < \infty \end{cases}$$

This is known as the NRT-dpa model and is the current international standard for quantifying radiation damage. The most prominent difference between the two models is the high energy behavior. While the constant number of defects in the Kinchin-Pease model is an underestimation, the NRT-dpa overestimates the number of stable defects by 300-400% [3]. K. Nordlund et al. therefore recently suggested an improved model including a point defect production efficiency function for the high energy interval of NRT-dpa [3]. Regardless of which model is used, the threshold displacement energy remains the key parameter for radiation damage estimation since its introduction to literature [6] in 1949.

1.1.3 Displacement cascades

Each displacement cascade is induced by energy transfer during a collision between a neutron (or other radiation particle) and a lattice atom referred to as the primary knock-on atom (PKA). Since lattices are not isotropic, atoms traveling in different directions behave differently. At high energies, atoms can be displaced long distances by channeling, movement inbetween atoms in open directions of a lattice. At low energies, channeling is not possible, instead displacements in high symmetry directions are characterized by binary collision chains between atoms at a straight line, with small energy transfer to surrounding atoms. Such sequences are referred to as replacement collision sequences (RCS), and occur frequently due to focusing, a geometrically induced phenomenon that focuses collision sequences near high symmetry directions [1]. In contrast, displacement cascades in low symmetry directions are characterized by chaotic motion and fast thermalization.

Due to the low energy transfer to surrounding atoms in replacement collision sequences, high energetic cascades often split into subcascades [1]. Through subcascade splitting, the mechanisms of high energetic cascades in the 10-20 keV PKA energy range can largely be studied by simulations of low energy cascades.

In conclusion, simulation of displacement cascades near the threshold displacement energy is of great importance for both the understanding and calculation of radiation damage. They provide understanding of the whole primary damage process in irradiated solid crystalline materials, and the related threshold displacement energy is the key factor for radiation damage calculations and component lifetime estimates.

1.1.4 Simulating defect formation

High energetic cascades may be studied, as mentioned before, by low energy cascades (through subcascade splitting). The low energy allows for relatively small supercells, which in turn allows for usage of the most precise methods, molecular dynamics (MD) simulations. However, it should be mentioned that high energetic cascades can be studied directly, for example through methods based on the binary collision approximation. Since the method only treats the two most high energetic atoms, it is fast enough for the huge supercells required, but it is not very precise. When possible, MD is therefore the first choice for radiation damage simulations.

MD simulations for low energy cascades and threshold displacement energy simulations can be based on various methods, both classical, empirical and quantum mechanical ones. EAM is a common semi-empiric method used for MD displacement cascades, including for determining threshold displacement energies. DFT is the only quantum simulation method that is fast and efficient enough to treat displacement cascades, and really only at the very low, near threshold end of the scale. Only a handful of studies have been published to date. Both DFT and EAM will be described in the next sections.

1.2 DFT and EAM as methods for MD displacement cascade simulations

Defect and atom displacement has been studied in various metals using both classical methods and quantum mechanics based ab initio DFT methods. For estimating the displacement energy, DFT has been shown to yield superior agreement with experimental data compared to EAM, in Fe, SiC, among others [7, 8]. Also, since DFT is an ab initio quantum simulation method, based on more fundamental principles than EAM, it is expected to give more reliable results. In fact, results from DFT simulations are often used as fitting parameters in the construction of EAM potentials [9, 7]. However, the high computational cost associated with ab initio methods restricts simulation boxes to small sizes, typically to a few hundred atoms.

1.3 Density functional theory (DFT)

Even though the Schrödinger equation cannot directly be solved for even a single metallic atom, and clearly not for the large systems required in displacement cascades, there are methods for making quantum mechanics based MD. One such method is density functional theory (DFT) which was presented in two papers, by Hohenberg and Kohn [10] in 1964 and by Kohn and Sham in 1965 [11]. In DFT, firstly, the dynamics may be separated into two separate subproblems: the electronic problem, and the ionic problem treating the movements of the nuclei. It is the quasistatic electron density that is determined quantum mechanically in DFT. The electronic and ionic subproblems are described in detail in appendix A.1. A shorter summary of DFT and EAM will follow in section 1.5.

1.4 Embedded atom method (EAM)

The embedded atom method is a classical semi-empirical model. In the embedded atom method [12], each atom is treated as an impurity in a host consisting of all other atoms. Whereas the core-core interactions are modeled with pair potentials, the influence of the host electron density is approximated as that of a locally uniform electron gas. The resulting expression for the total energy is

$$E_{\text{tot}} = \sum_i F_i(\rho_i) + \frac{1}{2} \sum_{i \neq j} V_{i,j}(R_{ij})$$

where ρ_i is the host electron density at site i (the impurity), F_i , the thereof generated embedding energy, and $V_{i,j}(R_{i,j})$ the pair potential between atom i and j with relative distance $R_{i,j}$. Some intervals of the pair potential have empirical but generic expressions, for example that of Littmark et al. [13] for short range repulsion, and others are fitted to properties of each specific compound. Remaining intervals that are difficult to motivate are often interpolated. Several empirical methods exist for modeling the electron density and embedding energy.

In practice, since the EAM method is largely based on empirical considerations, and since every EAM potential is constructed to mimic a set of selected properties, EAM potentials are not necessarily reliable for purposes not considered in the construction. Further restrictions, in addition to the poor transferability, include that EAM potentials are restricted to systems with two, or at most three elements.

1.5 DFT - EAM comparison

To summarize the differences between DFT and EAM, DFT is an ab initio (from first principles), quantum mechanical method, whereas EAM is a classical semi empirical method. For DFT, the electron density at each ionic step is computed self consistently by solving many one-electron Schrödinger equations for an effective potential. The electron density obtained in each step is used to produce a new effective potential, used in the next self consistency step. EAM instead uses a potential that is an explicit function of the atom positions, to compute the atomic forces. DFT is both more general than EAM, and can be expected to provide reliable results in new situations, without being dependent on empirical fits or associated experiments. On the other hand, the greatest advantage of the EAM method compared to DFT is that it is considerably much faster, at least about 6 orders of magnitude, excluding start-up time (reading input data etc.) and for the simulations in the present project. Here, a typical simulation of 648 W atoms (W_pv VASP PAW PBE potential) and 200 time steps required about 12000 core hours for DFT, and a few core seconds for EAM (excluding start-up time).

2 Methods

2.1 Simulation setup

Displacement cascade simulations were alternately carried out using DFT and EAM, and the results compared with simulations purely based on DFT and EAM respectively. As a first estimate of how well the alternated DFT-EAM simulations conform to pure DFT simulation, the dynamics was qualitatively compared through total kinetic energy analysis. Lastly, the threshold displacement energy was determined for three directions and compared for the different methods.

All simulations with alternating EAM-DFT were carried out by using EAM (throughout LAMMPS) for the first time steps, and switching to DFT (VASP) for the remaining simulation. The reason EAM was applied at the start, and not for example at the end of a simulation, was that the dynamics was believed to be more sensitive near equilibrium, close to thermalization, in the end of a simulation. Also, whether or not a certain defect configuration is stable is determined after the high energetic collisions have stopped, rather than in the beginning. Thus it was argued that using EAM for the beginning would affect the TDE the least. However, other combinations of EAM/DFT could be the topic of future study. Below in figure 1, a schematic diagram of the simulation setup is provided.

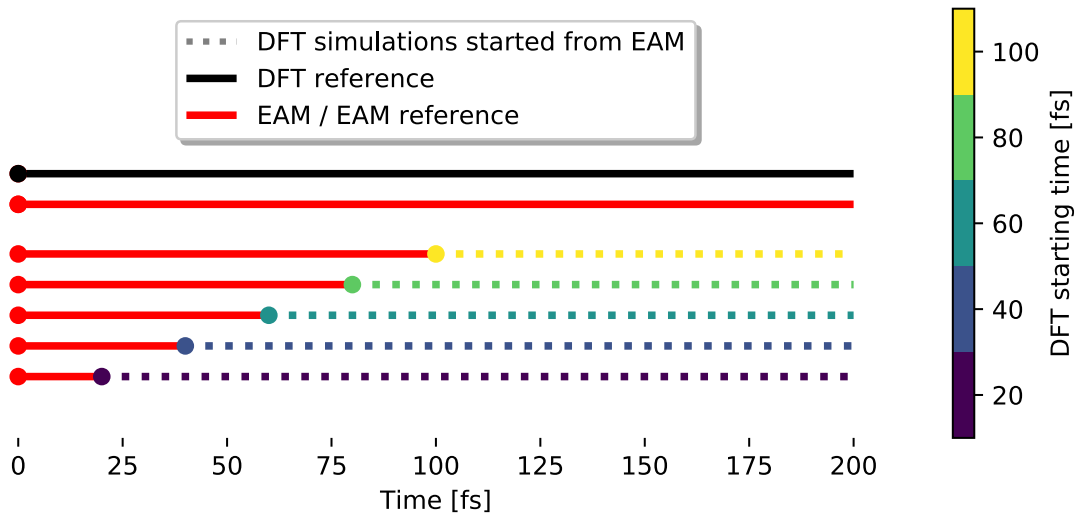


Figure 1: Schematic diagram of the simulation setup.

The dynamics for DFT, EAM and mixed DFT-EAM was analyzed for cascades in both low and high symmetry directions, and with energy near the threshold displacement energy. For the first qualitative comparison, the PKA was given an initial kinetic energy of 100 eV, and velocity in four different lattice directions; $\langle 100 \rangle$, $\langle 111 \rangle$, $\langle 110 \rangle$ and $\langle 135 \rangle$, see fig. 2 and 3. The threshold displacement energy was calculated for $\langle 110 \rangle$, $\langle 135 \rangle$ and $\langle 30, 5, 2 \rangle$. $\langle 110 \rangle$ is technically a high symmetry direction, but with fast thermalization making it similar to low symmetry directions as well. Furthermore, $\langle 135 \rangle$ is often chosen as an example low symmetry direction. The intention is that $\langle 135 \rangle$ will provide an indication of what can be expected in general for low symmetry directions. This certainly is a rough estimate, but should be sufficient for a first analysis, and a good tradeoff for computational cost.

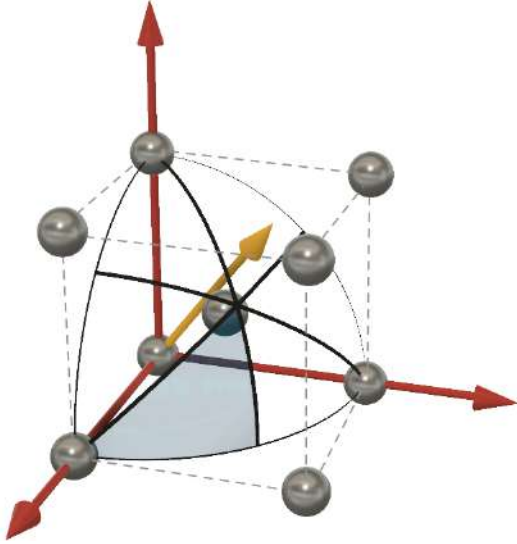


Figure 2: Lattice unit cell with sample lattice direction (yellow). Each triangle-shaped section of directions (black lines) is equivalent in a perfect crystal. Thus, the direction $\langle 135 \rangle$ (given in Miller indices) is for example equivalent to $\langle 531 \rangle$ and $\langle 351 \rangle$. The corresponding applies to other directions. The shaded section is shown in detail in figure 3.

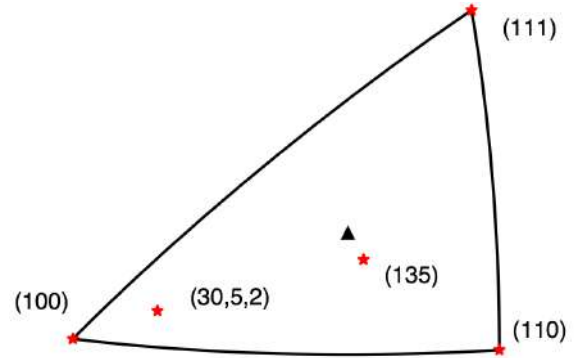


Figure 3: Irreducible direction spectrum showing the relation between lattice directions. The figure is a 2D-projection of the shaded section in fig. 2. The directions marked with red stars are investigated in the present study. The small black triangle is the projection direction (equal to the mean of the three corners).

2.2 Implementation

For the ab-initio DFT MD simulations, *Vienna Ab initio Simulation Package* (VASP) [14] was used. Furthermore, the EAM MD simulations were performed through *Large-scale Atomic/Molecular Massively Parallel Simulator*, LAMMPS [15]. Specifically, a tungsten EAM potential by Marinica et al. [9] was used, a potential developed for studying radiation defects and dislocations in tungsten. The code for switching between DFT and EAM simulation was here implemented in Python.

2.3 Choosing simulation parameters

DFT and EAM MD both require a set of parameters to be defined, including parameters related to discretization, boundary conditions, and some method specific parameters. Most simulations were conducted in a supercell of $9 \times 6 \times 6$ conventional unit cells of bcc tungsten (W) with periodic boundary conditions. Since each unit cell contains 2 atoms, the total number of atoms is 648. While a larger supercell would naturally give less self interference induced by the periodic boundary conditions, the larger number of atoms would also significantly increase the computational cost. At a minimum, the supercell should be large enough that the whole cascade is surrounded by at least one layer of low energetic atoms, so that the high energetic atoms in the cascade do not collide unphysically with high energetic atoms in any of the cascade's periodic images. The chosen size was considered a good compromise between computational cost and physical correctness, and all simulations were of appropriate energy or total time to avoid the aforementioned strong self interference. The elongated non-cubic supercell shape was selected to avoid unphysical dynamical self-interaction of a self-interstitial atom and the vacancy it has left behind in the particular case of the $\langle 111 \rangle$ replacement collision sequence.

2.3.1 Absolute convergence, ionic relaxation and choice of lattice constant

For accurate simulations, it is important to have a relaxed structure. The purpose of structure relaxation, in general, is to find the equilibrium atom positions, the positions that give the least total energy. For MD simulations, a relaxed structure is usually used for the initial positions, and for most simulations (constant volume MD), the volume is furthermore fixed and set equal to the volume of the relaxed structure. However, depending on method, the relaxed structure of a simulated system will differ. For example, the relaxed structure will be slightly different for DFT and EAM, and will also be different from the real, experimentally observed structure. One reasonable choice for getting a relaxed structure for the initial positions in a MD simulation is to use the structure that is relaxed according to the simulation method used for the actual simulations (cascades etc.), in this case DFT or EAM.

In this project, the DFT structure relaxation methods implemented in VASP were used to gain a relaxed structure close to absolute converged. Since the lattice type is known, and must be the same as for the real system, only volume (lattice constant) relaxation was considered necessary. Furthermore, the structure was relaxed for the primitive unit cell, statically (0 K), and the convergence of the total energy and lattice parameter was investigated with respect to number of \mathbf{k} -points and the maximum plane wave energy, E_{max} , both restricting the plane wave basis completeness. Remaining parameters that may affect the relaxation accuracy were chosen appropriately to give acceptable accuracy even for the highest investigated number of \mathbf{k} -points and E_{max} . The results are shown in figure (5) to (6). For details on the convergence parameters and relaxation methods, the reader is referred to the appendix and the VASP manual in ref. [16].

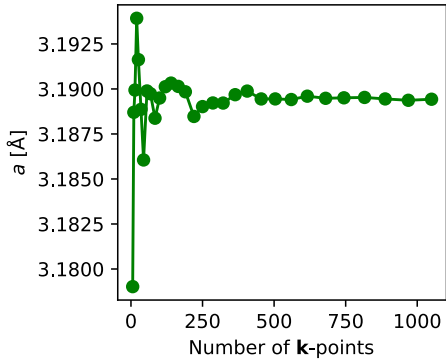


Figure 4: Lattice constant as function of number of \mathbf{k} -points, at $E_{max} = 700$ eV. The figure constitutes a detailed plot of the top row in figure (5).

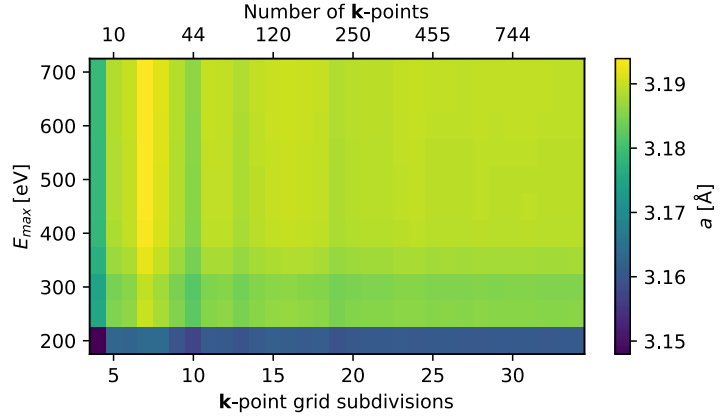


Figure 5: Lattice constant as function of number of \mathbf{k} -points and maximum plane wave energy, E_{max} . The number of \mathbf{k} -points is dependent on the \mathbf{k} -point grid subdivisions used for the \mathbf{k} -point grid construction, and thus the dual x-axis.

For readers familiar with VASP, each data point in fig. (4) to (6) was obtained through two consecutive volume relaxation procedures with $IBRION = 2$, $ISIF = 7$, in accordance with the VASP recommendations in ref. [10]. Note that the energy plotted here is not the energy obtained from the tetrahedron method ($ISMEAR = -5$) as described in ref. [10], but the energy of the last step of the structure relaxation. This is the energy obtained using the same smearing method as for all steps of the structure minimization, and for all MD cascade simulations in the present study, which is the energy of interest for the absolute convergence analysis.

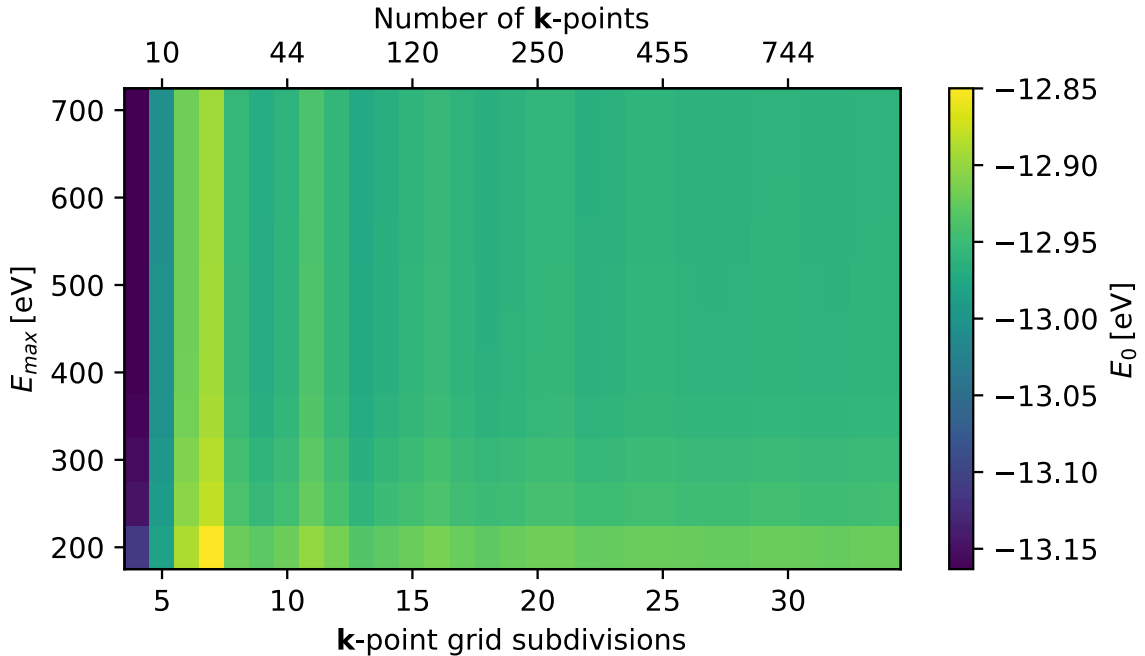


Figure 6: Energy convergence plot. Total energy for volumetric relaxed unit cell as function of maximum plane wave energy, E_{max} and number of \mathbf{k} -points. The number of \mathbf{k} -points is dependent on the \mathbf{k} -point grid subdivisions used for the \mathbf{k} -point grid construction, and thus the dual x-axis.

Even though many potentials and simulation methods give distinct lattice parameters for a given system, the lattice constant for the EAM simulations were set equal to that used for (and obtained from) DFT, in order to simplify calculations. Also note that several reasonable choices for the structure relaxation exist, for example to use the lattice parameter obtained by using the same supercell and simulation parameters as used in the MD-simulations. This would result in a different lattice parameter, relaxed for the actual system used in the MD-simulations, however not absolute converged. Also, when using a small basis set, the equilibrium structure might possibly incorrectly depend on positions of other atoms. Suspicions of this and similar issues motivated the choice of using a close to absolute converged lattice parameter.

Conclusions drawn from the structure relaxation were that both the total energy and lattice parameter for the structure relaxation appear to converge with respect to the plane wave basis completeness. The lattice parameter was chosen to be

$$a := 3.19 \text{ \AA}$$

which is a value approximately in accordance with the converged value of figure (4) and (5) (approximately 3.1895 \AA).

2.4 Evaluating alternating EAM-DFT qualitatively

For the first comparison between EAM, DFT and alternating EAM-DFT, the time evolution of the total kinetic energy was the main focus. The similarity of the total kinetic energy could be expected to be an indication of the overall similarity of the system's time evolution. The qualitative comparison through analysis of the total kinetic energy was complemented with 3D visualizations of the cascades (fig. 7) provided in OVITO [17].

The energy loss per collision was analyzed as in ref. [18]. The evolution of the energy loss per collision in RCS is strongly dependent on the potential [18] and can be used as a measure of similarity, particularly for replacement collision sequences due to the large number of collisions.

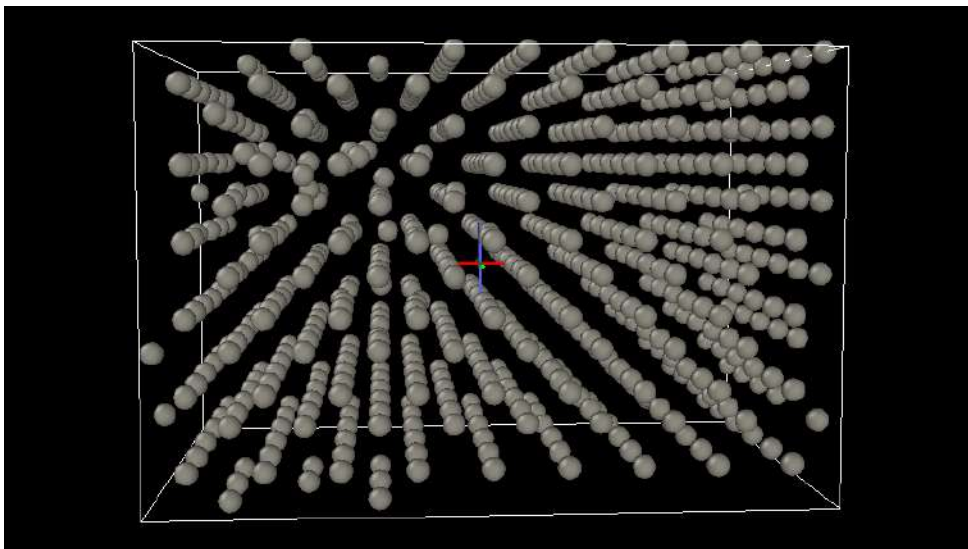


Figure 7: 3D visualization of a displacement cascade, provided in OVITO.

2.5 Comparing threshold displacement energy calculations

For a specific simulation method, the threshold displacement energy can be determined by performing sufficiently long cascade simulations with varying PKA energy and subsequently checking which energies that give stable defects. First, initial energy guesses are made until one energy below the TDE is found (with no stable defects), and one above the TDE (with a stable Frenkel pair). After that, the TDE is determined more precisely through binary search. To clarify, in the binary search, the energy interval for the TDE is reduced by bisection, iteratively testing an energy in the middle of the known interval obtained from last iteration step.

The simulation setup for the cascade simulations used for determining the TDE was similar to that used hitherto and demonstrated in fig. (1). However, the exception is that the 200 fs simulations were continued, using DFT and a longer time step of 3 fs instead of 1 fs. Longer time step can be justified by the fact that the maximum atom velocity has decreased significantly after 200 fs. For one direction, $\langle 110 \rangle$, EAM required a somewhat larger supercell because of high sensitivity for thermal self interaction for the particular defect configuration. For the regular $9 \times 6 \times 6$ supercell, the high thermal movements would cause recombination for the specific configuration of the Frenkel pair, for all reasonable energies. This should be considered a limitation of the EAM potential and should not affect the validity of analyses of the present work.

The TDE cascade simulations were stopped either if and when the defect pair recombined, or at a time considered sufficient to know with high certainty that the defect is stable. Mostly, the stability could be substantiated by observing that the interstitial changed configuration to the more stable, ground state configuration, the $\langle 111 \rangle$ crowdion interstitial [19], and that its distance to the vacancy was not too small (determined by experience). Most importantly, for the critical simulation corresponding to the smallest upper bound of the TDE intervals, it was always confirmed that the interstitial changed into the $\langle 111 \rangle$ crowdion configuration.

3 Results

3.1 Evaluating alternating EAM-DFT qualitatively

Displacement cascade simulations were alternately carried out using DFT and EAM, and the results compared with simulations purely based on DFT and EAM respectively, see figure 1 in methods. As a first estimate of how well the alternated DFT-EAM simulations conform to pure DFT simulation, the dynamics was qualitatively compared through total kinetic energy analysis. Lastly, the threshold displacement energy was determined for three directions and compared for the different methods. The most interesting and important results are given in section 3.2 to 3.4.

3.1.1 Verification of fundamental properties

As expected, for different PKA directions, the temporal evolution of the collision sequences differs significantly. In the high symmetry directions $\langle 100 \rangle$ (fig. 9 to 8), and particularly $\langle 111 \rangle$ (fig. 12 to 14), the energy loss per collision is notably smaller than in the low symmetry direction $\langle 135 \rangle$ (fig. 16) and $\langle 110 \rangle$ (fig. 15), since most of the energy is exchanged between few particles. By comparing the kinetic energy plots and 3D animation of the corresponding collision sequence, it could be observed that in $\langle 111 \rangle$ and $\langle 100 \rangle$, the total kinetic energy oscillates with the same periodicity as the collision sequence, and that two sets of points in the kinetic energy plot (8) correspond to well defined positions in the RCS. Firstly, the minima (green) coincides with when two atoms of the chain are the closest to each other, and the inflexion points with negative derivative (pink) are assumed approximately when the high energetic atom passes a window of four atoms that normally constitute four of the eight nearest neighbors (fig. 2).

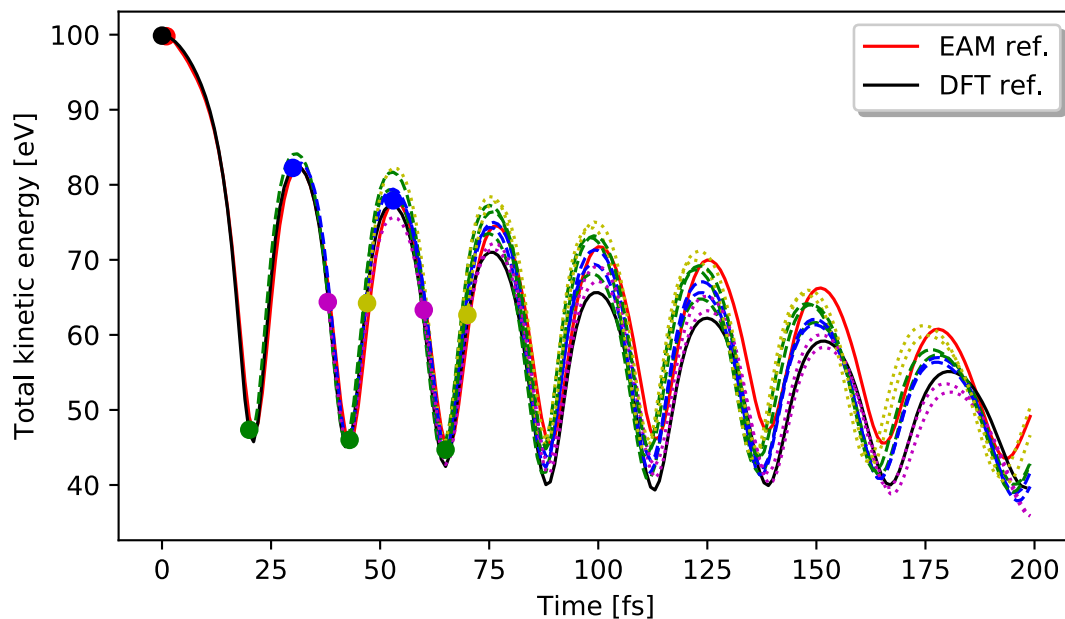


Figure 8: Total kinetic energy for RCS in $\langle 100 \rangle$ at 100 eV for sets of simulations with DFT starting at the same phase. Notice the similarity of simulations with the same DFT starting phase (same color). The figure demonstrates the importance of starting phase.

3.1.2 100 eV RCS in $\langle 100 \rangle$

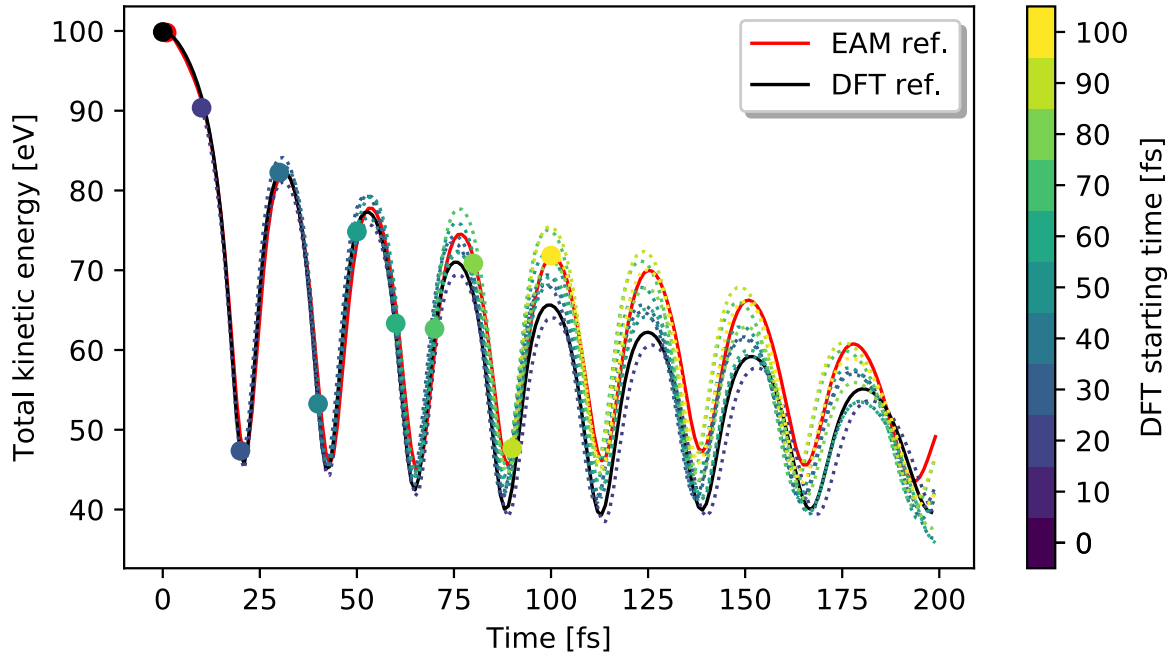


Figure 9: Total kinetic energy for RCS in $\langle 100 \rangle$ at 100 eV with VASP starting times between 0 and 100 fs.

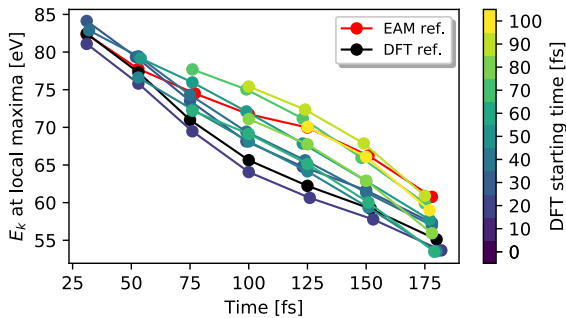


Figure 10: Local maxima of total kinetic energy for RCS in $\langle 100 \rangle$ at 100 eV.

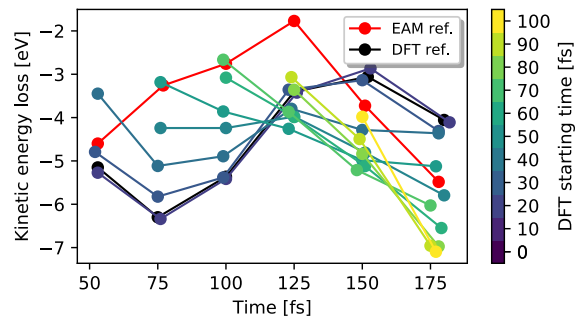


Figure 11: Kinetic energy loss per collision for RCS in $\langle 100 \rangle$ at 100 eV, equals the kinetic difference between two consecutive collisions. The value of a point at time t equals the kinetic energy difference between the local maxima p_n at time t , and the local maxima before that, p_{n-1} .

From the simulations in the $\langle 100 \rangle$ -direction, it can be observed that at a given time, generally, alternating EAM-DFT simulations with smaller DFT starting time are closer to the reference DFT simulation (black). Also, for many alternating EAM-DFT simulations, the kinetic energy appears to initially diverge from the reference DFT simulation. The simulations starting after up to about 60 fs are all fairly similar to the reference DFT simulation, compared to the EAM simulation, although the fairness certainly also depends on the desired accuracy.

3.1.3 100 eV RCS in $\langle 111 \rangle$

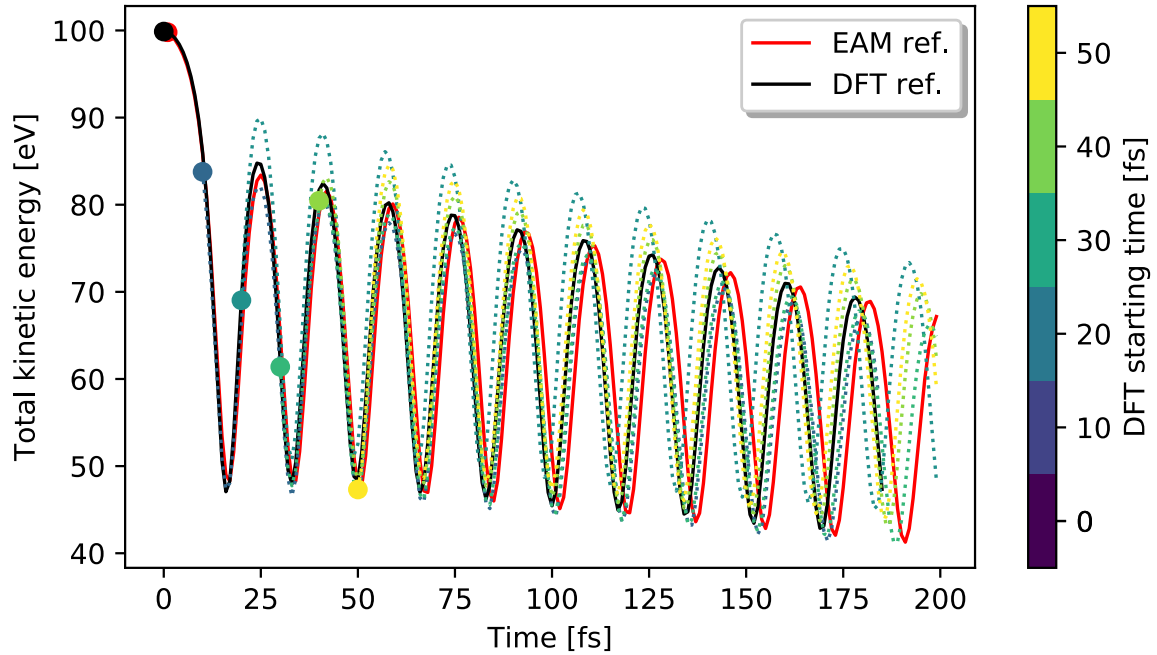


Figure 12: Total kinetic energy for RCS in $\langle 111 \rangle$ at 100 eV.

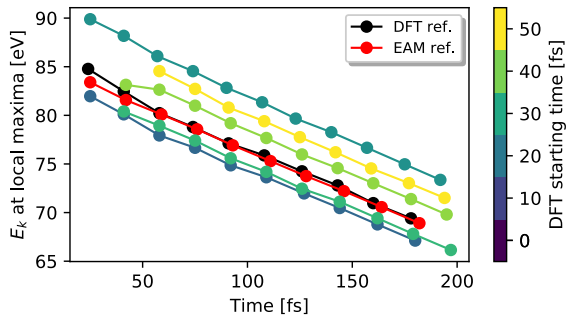


Figure 13: Local maxima for RCS in the $\langle 111 \rangle$ direction.

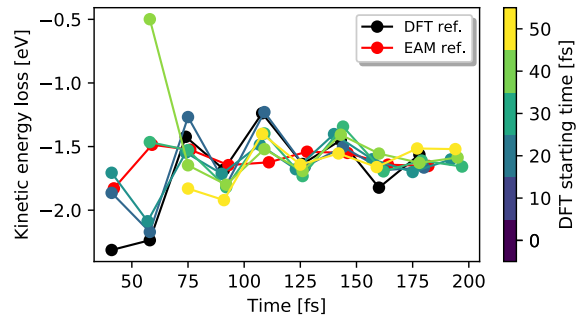


Figure 14: Energy loss per collision for RCS in the $\langle 111 \rangle$ direction.

The simulations in the $\langle 111 \rangle$ -direction share the same periodic behavior as in the $\langle 100 \rangle$ -direction. However, note that the error for each simulation is constant in time, as opposed to the simulations in the $\langle 100 \rangle$ -direction. Also, in general, the error does not seem to be smaller for smaller starting time, but rather possibly depend on the starting phase. Note that the EAM and DFT reference simulations are more similar to each other in most respects, than to the alternating EAM-DFT simulations. Furthermore, the energy loss per collision (14) is smaller than in $\langle 100 \rangle$.

3.1.4 100 eV RCS in $\langle 110 \rangle$

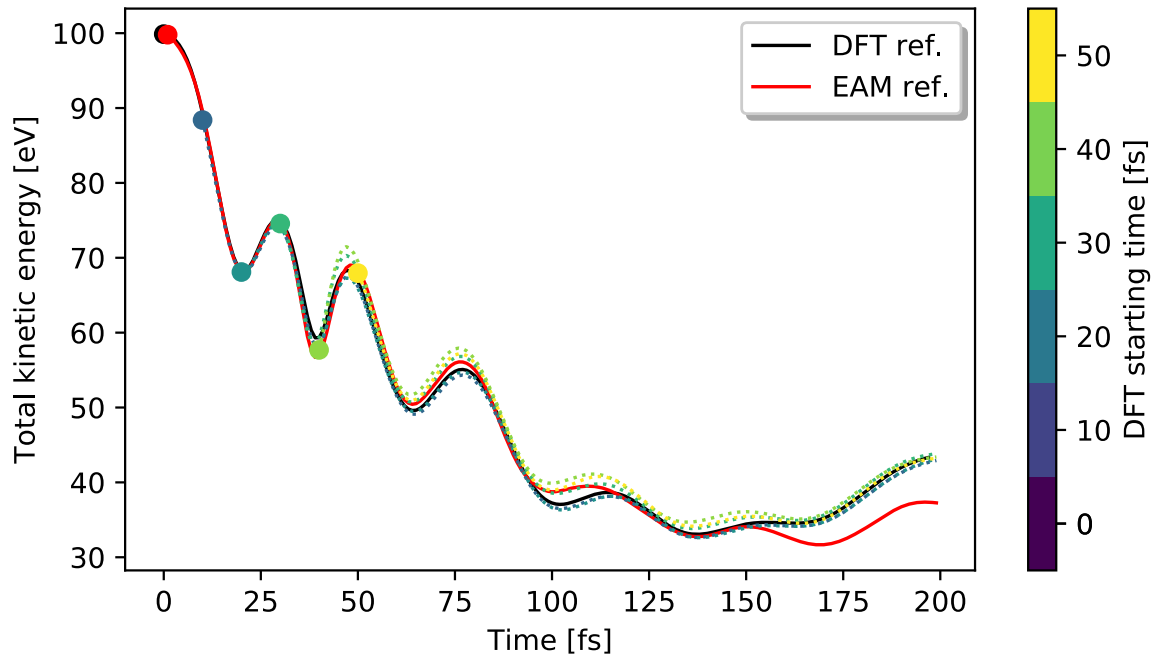


Figure 15: Total kinetic energy for RCS in $\langle 110 \rangle$ at 100 eV.

In the simulations with PKA direction $\langle 110 \rangle$, it can be observed that the errors diverge up to approximately 100 fs, after which the errors decrease. Since the kinetic energy decreases rather fast in the $\langle 110 \rangle$ direction, the replacement collision sequence ends after fewer collisions, here at time before 200 fs. Note that the pure EAM simulation diverges notably from the other simulations after 150 fs.

3.1.5 100 eV displacement cascade in $\langle 135 \rangle$

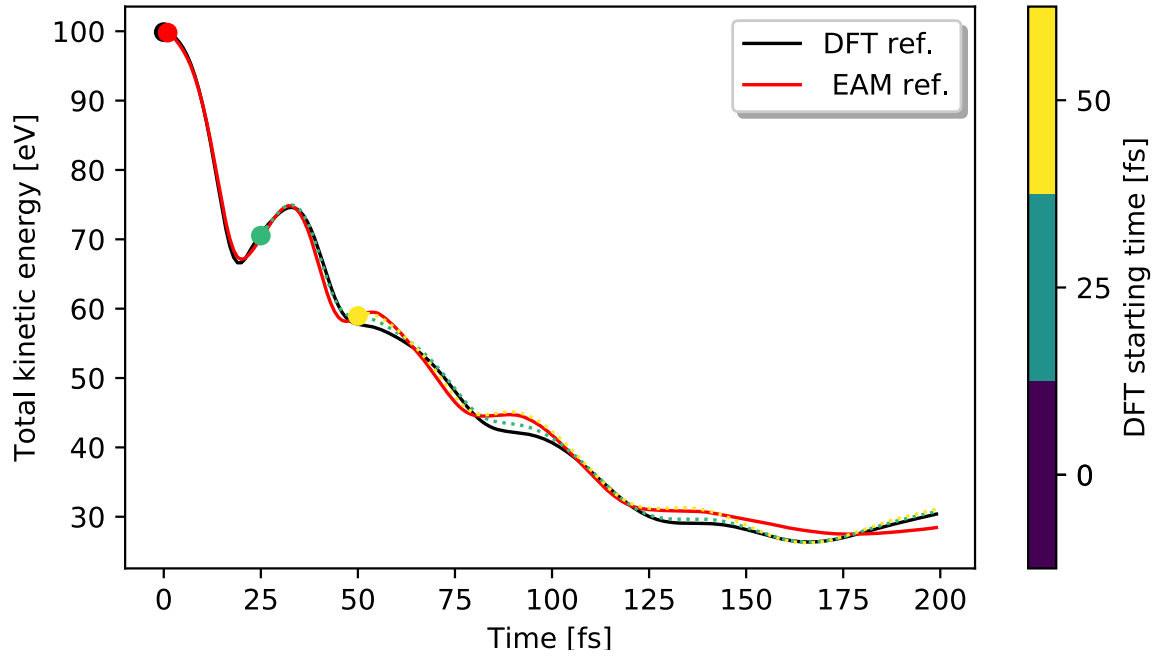


Figure 16: Total kinetic energy for RCS in $\langle 135 \rangle$ at 100 eV.

Similarly to the simulation in $\langle 110 \rangle$, the kinetic energy in $\langle 135 \rangle$ decreases fast. The differences between all methods are subtle, and all methods give similar kinetic energy time evolution, although the number of starting times tested for alternating EAM-DFT is rather limited. However, as in $\langle 110 \rangle$, the kinetic energy of alternating EAM-DFT appears to have better agreement with DFT than EAM in the last 50 fs of the 200 fs simulation interval, though it is not as clear as in $\langle 110 \rangle$.

3.2 Determination of TDE in $\langle 110 \rangle$

First, the TDE was determined using pure EAM and pure DFT. After that, the TDE was determined for the alternating EAM-DFT method, with DFT starting at 50, 100, 150 and 200 fs. For pure DFT, the TDE was determined to precision ± 0.5 eV, which required 7 simulations. In order to reduce the total simulation cost, the TDE for alternating EAM-DFT was however determined to precision ± 5 eV. The threshold displacement energy in $\langle 110 \rangle$ is given in table (1).

| Simulation method | TDE [eV] |
|------------------------|----------|
| EAM | 45 |
| DFT | 97 |
| DFT starting at 50 fs | 90-100 |
| DFT starting at 100 fs | 90-100 |
| DFT starting at 150 fs | 90-100 |
| DFT starting at 200 fs | 90-100 |

Table 1: Threshold displacement energy for replacement collision sequence in $\langle 110 \rangle$ from EAM, DFT, and alternating EAM-DFT.

The threshold displacement energy is more than twice as high for DFT as for EAM. Also, the TDE for alternating EAM-DFT is near the DFT value at between 90 eV and 100 eV (not determined more precisely).

3.3 Determination of TDE in $\langle 135 \rangle$ and $\langle 30, 5, 2 \rangle$

The threshold displacement energy in $\langle 135 \rangle$ and $\langle 30, 5, 2 \rangle$ was secondly determined, but somewhat less detailed than in $\langle 110 \rangle$. The threshold displacement energies are given in table (2).

| Simulation method | TDE in $\langle 135 \rangle$ [eV] | TDE in $\langle 2, 5, 30 \rangle$ [eV] |
|------------------------|-----------------------------------|--|
| EAM | 105 | 33 |
| DFT | >120 | 40 – 50 |
| DFT starting at 50 fs | - | > 40 |
| DFT starting at 100 fs | - | 30 – 40 |
| DFT starting at 150 fs | 115-120 | 30 – 40 |

Table 2: Threshold displacement energy for replacement collision sequence in $\langle 110 \rangle$ from EAM, DFT, and alternating EAM-DFT.

In $\langle 135 \rangle$, it can be observed that the TDE quite high for all methods, but that the DFT and alternating EAM-DFT values are higher than the EAM value, up to the precision of energy sampling. Furthermore, in $\langle 30, 5, 2 \rangle$ the TDE is small for all methods, but somewhat higher for DFT than for EAM and alternating EAM-DFT.

3.4 Simulation cost

The purpose of the method is to reduce time, and it is therefore relevant to make an estimate of the simulation cost reduction. The simulation times in core hours is given in table 3 and 4. The data is limited and should be seen as an example; the actual time savings is probably dependent on many factors, including the specific simulation parameters used, energy and direction. Simulation cost reduction would in other cases probably be both higher and lower than the values given here.

Since the simulations at energies above and below the TDE have different stopping conditions, the typical required physical time differs, more specifically approximately a factor 2 for the parameters and considerations made. Therefore, the simulation time for an energy above and an energy below the TDE is given for the typical physical time required above and below the TDE, respectively.

| DFT starting time [fs] | Simulation cost (750 fs cascade) [core h] | Part of pure DFT cost |
|---------------------------|--|--------------------------|
| 0 | 12650 | 100% |
| 50 | 11660 | 92% |
| 100 | 8230 | 65% |
| 150 | 4990 | 39% |
| 200 | 1590 | 1/8 |

Table 3: Simulation cost for DFT and alternating EAM-DFT. The values are for simulations in $\langle 110 \rangle$ with PKA energy *below* the TDE and for the corresponding required physical time of 750 fs. The simulations based purely on DFT have DFT starting time 0 fs. EAM has comparatively negligible simulation cost.

| DFT starting time [fs] | Simulation cost (1400 fs cascade) [core h] | Part of pure DFT cost |
|---------------------------|---|--------------------------|
| 0 | 16390 | 100% |
| 50 | 23140 | 141% |
| 100 | 10200 | 62% |
| 150 | 6230 | 38% |
| 200 | 3390 | 1/5 |

Table 4: Simulation cost for DFT and alternating EAM-DFT. The values are for simulations in $\langle 110 \rangle$ with PKA energy *above* the TDE, and for the corresponding required physical time of 1400 fs. The simulations based purely on DFT have DFT starting time 0 fs. EAM has comparatively negligible simulation cost.

The simulation time of MD cascade simulations is dependent on mainly two factors, the number of ionic steps (commonly referred to as time steps), and the number of electronic self consistency steps required for convergence in each ionic step.

As seen in table 3 and 4, the time reduction compared to pure DFT varies greatly depending on the DFT starting time for the alternating EAM-DFT method. For small DFT starting times, the time reduction is unexpectedly small, but it is also unexpectedly large for large starting times. Typically, the number of electronic self consistency steps was either around the preset maximum of 60, in the beginning of cascades, or between 4 and 7, some time after the initial PKA - neutron collision. The physical time for the transition from many to few electronic steps varied greatly and was method dependent. Alternating EAM-DFT simulations with small DFT starting time remained for most of the simulation at 50-60 electronic self consistency steps, and the extreme example is the alternating EAM-DFT simulation in table 4 with 50 fs starting and energy above the TDE, which was slower than the simulation based purely on DFT. In contrast, the number of electronic self consistency steps in alternating EAM-DFT simulations with 200 fs starting time was consistently between 4 and 7 throughout the DFT part of the simulation. The resulting simulation cost is 1/5 and 1/8 of the pure DFT simulation cost, for energy above and below the TDE respectively.

4 Discussion

In the present study, we asked whether it would be possible to substitute parts of a molecular dynamics simulation based on the more accurate DFT method, for the less computationally costly EAM-method. The EAM poses a number of limitations and considerations must be undertaken to evaluate under what circumstances losses to computational accuracy are tolerable. The qualitative kinetic energy analysis, and the quantitative threshold displacement energy determinations have provided some insights into this.

4.1 Evaluating alternating EAM-DFT qualitatively

The purpose of the qualitative kinetic energy analysis of displacement cascades was to get a first estimate of what could be expected of the suggested alternating EAM-DFT method. For all PKA directions, the alternating EAM-DFT method had good agreement to the pure DFT. However, in $\langle 100 \rangle$, it was demonstrated that the specific starting point in the periods of the RCS (i.e. the phase) has influence on the similarity to pure DFT simulation in high-symmetry replacement collision sequences, with respect to the kinetic energy time evolution. Also, in $\langle 111 \rangle$, the kinetic energy time evolution was quite similar between DFT and EAM, more similar than between DFT and alternating EAM-DFT. The kinetic energy error of alternating EAM-DFT was however constant over time and only introduced in the EAM-DFT transition.

The fact that the alternating EAM-DFT method appeared to agree well with DFT, and that EAM and DFT are similar up to at least 150-200 fs, indicated that at least the first 150 to 200 fs of a DFT MD cascade could possibly be substituted to EAM with little loss of accuracy. This motivated spending more supercomputer time on further investigation into the accuracy of the alternating EAM-DFT method, more specifically through the actual sample TDE computations later presented in section (3.2).

4.2 Determination of TDE in $\langle 110 \rangle$

In $\langle 110 \rangle$, the TDE was considerably higher for DFT than for EAM, and the alternating EAM-DFT was for all DFT starting times verified to give TDE with good agreement with the DFT value. The reason for the large TDE discrepancy between DFT and EAM seemed to be that the recombination distance was longer for DFT than EAM. In other words, the defect pair created at the TDE of EAM would not be stable in DFT. Also, the interstitial formed at the TDE was of different kind for DFT and EAM (but the same for alternating EAM-DFT and DFT). For DFT and alternating EAM-DFT, the interstitial evolved into the $\langle 111 \rangle$ crowdion interstitial, whereas for EAM, the interstitial was a $\langle 110 \rangle$ dumbbell. The reason that alternating DFT-EAM had such good agreement with DFT could therefore be that whether or not a specific defect is stable is largely determined sometime after the first say 200 fs, when DFT was applied and not EAM. It seems that the properties of EAM are sufficiently good for high energetic collisions, but lack the accuracy needed to accurately predict whether or not a defect is stable.

This kind of differences constitute one of the main reasons why more accurate methods than EAM are needed. Even quite small details in the EAM potentials have great effect on the behavior, making them unreliable. It is also remarkable considering the particular EAM potential used here was developed for defect and radiation damage studies.

4.3 Determination of TDE in $\langle 135 \rangle$ and $\langle 30, 5, 2 \rangle$

The direction $\langle 135 \rangle$ is often chosen as a typical low symmetry direction. $\langle 30, 5, 2 \rangle$ was chosen as a border direction near the high symmetry direction $\langle 100 \rangle$. It is a direction on the border to focusing towards the $\langle 100 \rangle$ direction, and therefore differences between the methods could be prominent. However, for both $\langle 135 \rangle$ and $\langle 30, 5, 2 \rangle$, the TDE seemed relatively equal for all methods. In $\langle 135 \rangle$, the TDE was high for all methods (>100 eV), while for all methods it was in the low end of the scale for $\langle 30, 5, 2 \rangle$.

4.4 Limitations and topics of future study

High computational cost of DFT restricted the number of directions tested for the qualitative kinetic energy and TDE comparison. The TDE for the high symmetry directions $\langle 111 \rangle$, and $\langle 100 \rangle$, was thus not analyzed since replacement collision sequences (RCS) are quite long at the TDE. The length should not inherently be problematic for the alternating EAM-DFT method. On the contrary, the similarities between EAM and DFT observed in the 200 fs long kinetic energy comparison simulations is an indication that more than the first 200 fs DFT may be substituted for EAM with small resulting TDE discrepancy. This is particularly probable for $\langle 111 \rangle$, which showed the greatest similarity between DFT and EAM in the kinetic energy comparison. This direction is also important due to the large span of lattice directions that through focusing induce RCS:s in $\langle 111 \rangle$. The reason that TDE was not calculated for $\langle 111 \rangle$ was instead that the pure DFT simulations for the comparison need to be rather long, and with high computational cost through most simulation since the maximum atom kinetic energy is high for a long time, requiring short time steps and many electronic self consistency steps (slow convergence). Also, the $\langle 111 \rangle$ direction is particularly sensitive to the thermal movements due to the high symmetry, and would thus require multiple simulations for the same energy, increasing the computational cost for the analysis further. The restrictions of the present project did unfortunately not allow for such time consuming simulations, but it would be interesting to investigate in future studies.

5 Conclusions

Judging by the five crystallographic directions considered, the first part of a DFT simulation can be substituted for EAM, without significant loss in the predictive power of DFT, but with greatly reduced simulation cost. Based on the TDE comparison, the appropriate length that can be substituted appears direction dependent, but for low symmetry directions, it can potentially be as long as 200 fs. The corresponding simulation cost is reduced to 1/5 - 1/8 compared to simulation based purely on DFT for the example direction $\langle 110 \rangle$. From the qualitative kinetic energy analysis, we argue that more time could be substitutable in the high symmetry directions $\langle 100 \rangle$ and especially $\langle 111 \rangle$, due to the high similarity regarding kinetic energy time evolution and due to the high regularity of the dynamics. This reasoning includes the relatively large span of directions that due to focusing induces RCS:s in $\langle 111 \rangle$ and $\langle 100 \rangle$. We hope that our work can also inspire work in other domains where DFT use today is limited due to its high computational cost; that with informed selection of alternation conditions, substantial improvement in accuracy and computation time can be obtained.

References

- [1] G.S. Was. *Fundamentals of Radiation Materials Science: Metals and Alloys*; Springer: Berlin, Germany, 2007. Pages 91, 103, 104, 207, 218, 232, 267, 273, 597, 626, 643, 711, 725, 726, 736.
- [2] S.J.Zinkle. Radiation-Induced Effects on Microstructure. *Comprehensive Nuclear Materials*, vol. 1, Elsevier Ltd, 2012, pp. 65–98.
- [3] K. Nordlund et al. Improving atomic displacement and replacement calculations with physically realistic damage models. *Nat Commun.* 2018 Mar 14;9(1):1084.
- [4] G. H Kinchin and. R.S. Pease. The displacement of atoms in solids. *Rep. Prog. Phys.* 18, 1–51 (1955).
- [5] M. J. Norgett, M. T. Robinson & I. M Torrens. A proposed method of calculating displacement dose rates. *Nucl. Eng. Des.* 33, 50–54 (1975).
- [6] F. Seitz. On the disordering of solids by action of fast massive particles. *Disc Faraday Soc.* 5:271 (1949).
- [7] P. Olsson, C. S. Becquart & C. Domain. Ab initio threshold displacement energies in iron. *Mat. Res. Let.* 4:4 p219 (2016).
- [8] G. Lucas and L. Pizzagalli. Comparison of threshold displacement energies in β -SiC determined by classical potentials and ab initio calculations. *Nucl. Instrum. Methods Phys. Res. B* 229:p255 (2005).
- [9] M-C Marinica et al. Interatomic potentials for modelling radiation defects and dislocations in tungsten. *J. phys. cond. mat.* 25:p.395502 (2013).
- [10] P. Hohenberg and W.Kohn. *Phys. Rev.*, 136B:864 (1964).
- [11] W. Kohn and L.J. Sham. Self-Consistent Equations Including Exchange and Correlation Effects. *Phys. rev.*, 140:A1133 (1965).
- [12] M.S. Daw and M.I. Baskes. *Phys. rev. B*, 29:6443 (1984).
- [13] U.Littmark J.F. Ziegler, J.P. Biersack. *The stopping and Range of Ions in Solids. Pergamon Press, New York (1985).*
- [14] G. Kresse, J. Hafner. Ab initio molecular dynamics for liquid metals. *Phys. Rev. B.* 47:558 (1993).
- [15] S. Plimpton. Fast Parallel Algorithms for Short-Range Molecular Dynamics. *J Comp Phys*, 117, 1-19 (1995). <https://lammps.sandia.gov/>
- [16] G. Kresse, M. Marsman, and J. Furthmüller. “VASP the Guide” [PDF file]. Retrieved from <https://cms.mpi.univie.ac.at/vasp/vasp.pdf>
- [17] A. Stukowski. Visualization and analysis of atomistic simulation data with OVITO - the Open Visualization Tool. *Modelling Simul. Mater. Sci. Eng.* 18 (2010), 015012. <http://ovito.org/>

- [18] C.S. Becquart, A. Souidi and M. Hou Replacement collision and focuson sequences revisited by full molecular dynamics and its binary collision approximation, *Philosophical Magazine*, 85:4-7, 409-415, (2005).
- [19] P. M. Derlet, D. Nguyen-Manh, and S. L. Dudarev. Multiscale modeling of crowdion and vacancy defects in body-centered-cubic transition metals. *Phys. Rev. B* 76:054107 (2007).
- [20] J.P. Hansen and I.R. McDonald. *Theory of simple liquids, 2:nd Ed.* Academic (1969).
- [21] F. Bloch. Über die Quantenmechanik der Elektronen in Kristallgittern. *Z. Physik* 52:555 (1928).
- [22] F. Bloch. *Memories of Electrons in Crystals. Proc. R. Soc. Lond. A* 371, 24-27 (1980).
- [23] G. Floquet, *Ann. Sci. Ecole Norm. Sup.* , 12:2 pp. 47–88 (1883).
- [24] C. Kittel. *Introduction to Solid State Physics.* New York: Wiley (1996).
- [25] A. Eichler. “Sampling the Brillouin-zone”[PDF file]. Universität Wien . Retrieved from <https://www.vasp.at/vasp-workshop/slides/k-points.pdf>
- [26] U. von Barth, and C. D. Gelatt, *Phys. Rev. B* 21:2222 (1980).
- [27] P.E. Blöchl. Projector augmented wave method. *Phys. Rev. B* 50:17953 (1994).

A Appendix

A.1 Density functional theory

A.1.1 Ionic problem

For the ionic problem, it is reasonable to assume that the wave properties of the atom cores can be neglected if the de Broglie thermal wave length,

$$\lambda_B = \sqrt{\frac{2\pi\hbar^2}{mk_B T}} \quad (1)$$

is much smaller than the mean atomic distance [20]. For tungsten atoms at 300 K, this corresponds to a distance of 0.074 Å, which is much smaller even than the nearest neighbor distance, ~ 2.2 Å. For DFT in general, this assumption is made, and the ions (atom cores) are thus treated classically according to newton mechanics,

$$m\dot{\mathbf{r}}; = -\nabla V(\mathbf{r})$$

It is not uncommon that in MD simulations, many atoms are initially stationary. Inserting $T = 0\text{K}$ in (1) causes obvious problems, however, the validity of such simulations could be motivated by that all the important dynamics involve non stationary atoms with kinetic energies corresponding to sufficiently high temperature.

A.1.2 Electronic problem

In the electronic problem, the electrons are treated quantum mechanically. In the Born Oppenheimer approximation, the electronic Hamiltonian can be written

$$\hat{H}_e = \hat{T} + \hat{V}_{\text{int}} + \hat{V}_{\text{ext}}$$

where \hat{T} is the electron kinetic energy operator, \hat{V}_{int} is the electron-electron interaction and \hat{V}_{ext} is the nuclei-electron interaction. The corresponding scalar potentials V_{int} and V_{ext} are commonly referred to as the internal and external potential, respectively.

The Hohenberg Kohn theorems [10] provide a relationship between the ground state electron density $n(\bar{r})$, the external potential V_{ext} , and the total energy $E(n)$. Specifically, they state that

1. V_{ext} is a unique function of $n(\bar{r})$, except for a constant.
2. For a given V_{ext} , the total energy $E(n)$ assumes its minimal value for the correct $n(\bar{r})$.

The most important consequence of the Hohenberg Kohn theorems is that the many particle ground state is fully and uniquely determined by the electron density, which in turn may be determined by minimizing the total energy functional $E[n]$. Since the explicit expression of the many particle Hamiltonian (of real, interacting electrons) is unknown, the theorem cannot be used directly. However, Kohn and Sham [11] provided means of using the theorem in practice by transferring the exchange and correlation effects of the Hamiltonian of an interacting electron gas, to an effective potential of a corresponding non-interacting system. The resulting self consistent equations are the Kohn-Sham equations [11], and the proof thereof may be summarized as follows:

The total electric energy can be written

$$E[n] = \langle \Psi | \hat{T} + \hat{V}_{\text{int}} + \hat{V}_{\text{ext}} | \Psi \rangle = T + V_{\text{int}} + V_{\text{ext}} \quad (2)$$

Next, the total energy functional is written in terms of quantities of a corresponding non-interacting system (same electron density and external potential) of non-interacting electrons (primed variables):

$$E[n] = T + V_{\text{int}} + V_{\text{ext}} = T' + V'_{\text{int}} + V'_{\text{ext}} - [(T - T') + (V_{\text{int}} - V'_{\text{int}}) + (V_{\text{ext}} - V'_{\text{ext}})]$$

Here, for the non-interacting system, $V_{\text{ext}} = V'_{\text{ext}} = \int v_{\text{ext}}(\mathbf{r})n(\mathbf{r})d\mathbf{r}$ and $V'_{\text{int}} = \frac{1}{2} \iint \frac{n(\mathbf{r}_1)n(\mathbf{r}_2)}{|\mathbf{r}_1 - \mathbf{r}_2|} d\mathbf{r}_1 d\mathbf{r}_2$ are known. By defining $E_{\text{xc}} = (T - T') + (V_{\text{int}} - V'_{\text{int}})$ equation (2) may be rewritten as

$$E[n] = T' + \int V_{\text{ext}}(\mathbf{r})n(\mathbf{r})d\mathbf{r} + \frac{1}{2} \iint \frac{n(\mathbf{r}_1)n(\mathbf{r}_2)}{|\mathbf{r}_1 - \mathbf{r}_2|} d\mathbf{r}_1 d\mathbf{r}_2 + E_{\text{xc}}$$

Since the ground state is determined by $n(\bar{r})$, E_{xc} is a functional of $n(\bar{r})$,

$$E_{\text{xc}} = \int v_{\text{xc}}(\mathbf{r})n(\mathbf{r})d\mathbf{r}$$

for some unknown function $v_{\text{xc}}(\mathbf{r})$. $E[n]$ can then be written as

$$\begin{aligned} E[n] &= T' + \int V_{\text{ext}}(\mathbf{r})n(\mathbf{r})d\mathbf{r} + \frac{1}{2} \iint \frac{n(\mathbf{r})n'(\mathbf{r}')}{|\mathbf{r} - \mathbf{r}'|} d\mathbf{r} d\mathbf{r}' + \int v_{\text{xc}}(\mathbf{r})n(\mathbf{r})d\mathbf{r} \\ &= \int \left[v_{\text{ext}}(\mathbf{r}) + \int \frac{n'(\mathbf{r}_2)}{|\mathbf{r} - \mathbf{r}_2|} d\mathbf{r}_2 + v_{\text{xc}}(\mathbf{r}) \right] n(\mathbf{r})d\mathbf{r} \\ &= T' + \int v_{\text{eff}}(\mathbf{r})n(\mathbf{r})d\mathbf{r} = \sum_i \langle \psi_i | \hat{T}' + \hat{V}_{\text{eff}} | \psi_i \rangle \end{aligned}$$

In other words, the energy of the real system equals the energy of an imaginary system, of equal electron density and in an effective potential

$$v_{\text{eff}} = v_{\text{ext}}(\mathbf{r}) + \int \frac{n(\mathbf{r}_2)}{|\mathbf{r} - \mathbf{r}_2|} d\mathbf{r}_2 + v_{\text{xc}}(\mathbf{r})n(\mathbf{r})d\mathbf{r}$$

According to the variational principle, the energy of the non interacting system (and thus the energy of the interacting system) is minimized for the ground state of the non interacting system, given by the one particle Schrödinger equations

$$\left[-\frac{1}{2}\nabla^2 + V_{\text{eff}} \right] \psi_i = \epsilon_i \psi_i$$

Using that $n(\mathbf{r}) = \sum |\psi_i(\mathbf{r})|^2$, the Kohn-Sham equations are

$$\begin{aligned} v_{\text{eff}} &= v_{\text{ext}}(\mathbf{r}) + \int \frac{n(\mathbf{r}_2)}{|\mathbf{r} - \mathbf{r}_2|} d\mathbf{r}_2 + v_{\text{xc}}(\mathbf{r})n(\mathbf{r}) \\ \left[-\frac{1}{2}\nabla^2 + \hat{V}_{\text{eff}} \right] \psi_i &= \epsilon_i \psi_i \\ n(\mathbf{r}) &= \sum |\psi_i(\mathbf{r})|^2 \end{aligned} \quad (3)$$

These may be solved self consistently from top to bottom by guessing an initial electron density $n(\mathbf{r})$. Note that the system still contains an unknown exchange-correlating functional, though, in a more practical form than in the many particle Hamiltonian. In the paper by Kohn and Sham in which the Kohn Sham equations were originally derived, ref. [11], one approximation for v_{xc} was presented where the exchange-correlation energy is locally approximated as that of a uniform electron gas of the same density,

$$v_{\text{xc}}(\mathbf{r}) = \epsilon_{\text{xc}}(n(\mathbf{r})) \quad (4)$$

Equation (4) is the local density approximation (LDA). The LDA, which is DFT at its simplest form, predicts many properties of most compounds accurately despite its simplicity. In a more accurate approximation, the magnitude of the gradient of the electron density is included, resulting in the generalized gradient approximation (GGA),

$$v_{\text{xc}}(\mathbf{r}) = \epsilon_{\text{xc}}(n(\mathbf{r}), |\nabla n(\mathbf{r})|)$$

To solve the one electron Schrödinger equations efficiently, there are many possible simplifications due to the applied restrictions (periodic boundary conditions etc.), physical considerations, and wave function basis choice. The following sections will provide a brief description of some of them.

A.1.3 Bloch's theorem

In a periodic potential, the solutions of the Schrödinger equation are restricted to particular forms. F. Bloch found in 1928 that the eigenstates are products of a plane wave and a lattice periodic function [21], although an analogous but purely mathematical result was derived earlier by Gaston Floquet in 1883 [22, 23].

By assuming that the (locally defined) potential is translation symmetric, that is

$$V(\mathbf{r}) = V(\mathbf{r} + g_1 \mathbf{a}_1 + g_2 \mathbf{a}_2 + g_3 \mathbf{a}_3)$$

, for any $g_1, g_2, g_3 \in \mathbb{Z}$ compatible with the crystal size, Bloch showed that the eigenfunctions can be written

$$\psi_{klm}(x, y, z) = e^{2\pi i(\frac{kx}{a_1g_1} + \frac{ly}{a_2g_2} + \frac{mz}{a_3g_3})} u_{klm}(x, y, z) \quad (5)$$

where u_{klm} is a function with the same periodicity as the potential. Since (5) is valid for any translation coefficients g_1, g_2, g_3 compatible with the size of the whole crystal, in the macroscopic limit, the coefficients $\frac{2\pi k}{g_1}, \frac{2\pi l}{g_2}, \frac{2\pi m}{g_3}$ are arbitrary rational numbers, which can be approximated as arbitrary real numbers. In vector notation with $\mathbf{k} := \frac{2\pi k}{a_1g_1} \mathbf{a}_1 + \frac{2\pi l}{a_2g_2} \mathbf{a}_2 + \frac{2\pi m}{a_3g_3} \mathbf{a}_3$, (5) can be written

$$\psi_{\mathbf{k}} = e^{i\mathbf{k}\mathbf{r}} u_{\mathbf{k}}$$

where \mathbf{k} is an arbitrary vector in three dimensional real space.

Even though Bloch assumed a lattice with orthogonal basis vectors, the theorem holds in general [24]. Fourier expansion of $u_{\mathbf{k}}$ gives

$$\psi_j(\mathbf{k}, \mathbf{r}) = \sum_{\mathbf{G}} C_{j,\mathbf{k},\mathbf{G}} e^{i(\mathbf{k}+\mathbf{G})\mathbf{r}} \quad (6)$$

Note that \mathbf{G} is reciprocal lattice vectors due to the periodicity of u_k . Thus, any wave function solution to (3) can be written in terms of the eigenstates (6), and non periodic systems, such as those in displacement cascades, may be approximated as periodic systems by using large supercells i.e. periodicity at larger scales than the conventional and primitive unit cell. Note that the probability density $|\psi_j(\mathbf{k}, \mathbf{r})|^2$ is as expected, lattice periodic, with the same periodicity as the unit cell or supercell. To get the full solution, (6) has to be solved for all j , \mathbf{k} (or \mathbf{r}) and \mathbf{G} , and numeric computations naturally require appropriate discretization and sampling.

A.1.4 Brillouin zone (\mathbf{k}) sampling

Since the reciprocal and lattice $\{\mathbf{G}\}$ satisfies $e^{i\mathbf{G}\mathbf{R}} = 1$, where $\{\mathbf{R}\}$ is the direct lattice, plane waves in (6) that differ only by a reciprocal lattice vector are equivalent. Thus, for sampling k -space, it is sufficient to sample the first Brillouin zone. For a cuboid supercell, the first Brillouin zone is small and technically the Brillouin zone of a simple orthorhombic lattice, the supercell together with the periodic boundary conditions constitutes a simple orthorhombic lattice with rather complicated atoms basis. Because of the inverse relation between simulation cell and Brillouin zone size, treating just one \mathbf{k} -point, the gamma point, is often sufficient for large supercells [25].

A.1.5 Plane wave (\mathbf{G}) sampling

For each \mathbf{k} -point, there is an infinite number of plane waves corresponding to different \mathbf{G} -points. Since the wave function oscillates most at the core region, an approximation implemented in VASP [14] is to choose a basis for the wave function in the interstitial region consisting of waves that fulfill

$$\frac{\hbar^2}{2m} |\mathbf{G} + \mathbf{k}| < E_{\text{cut}}$$

for an energy cutoff E_{cut} [16]. The core region, where the wave function generally has higher frequencies, is typically treated separately, see the PAW-method below.

For accurate numeric calculations, the number of terms in the serial expansion has to be restricted to a finite (and unlike the original set, bounded) subset of \mathbf{G} -vectors corresponding to the physically most important plane waves. U. von Barth et al. showed that the strong oscillations are due to core states and of less significance for the interatomic interactions [26].

A.1.6 The PAW-method

There are several ways of representing the wave function for effective and accurate computations, and one of the more common is the projector augmented wave method (PAW) [27]. It is based on plane wave expansions in the interstitial region, with atomic orbitals in the core region.